Computational Materials Science 207 (2022) 111302

Contents lists available at ScienceDirect

Computational Materials Science

journal homepage: www.elsevier.com/locate/commatsci

Full length article

High-throughput generation of potential energy surfaces for solid interfaces

Michael Wolloch [a,*], Gabriele Losi [b], Omar Chehaimi [b], Firat Yalcin [a], Mauro Ferrario [c], Maria Clelia Righi [b,*]

[a] Computational Materials Physics, Faculty of Physics, University of Vienna, Kolingasse 14-16, 1090, Vienna, Austria
[b] Department of Physics and Astronomy, Alma Mater Studiorum University of Bologna, 40127 Bologna, Italy
[c] Dipartimento di Scienze Fisiche, Informatiche e Matematiche, Università di Modena e Reggio Emilia, Via Campi 213/A, 41125, Modena, Italy

ARTICLE INFO

Keywords:
High-throughput
Interfaces
Potential energy surface
Density functional theory
Tribology

ABSTRACT

A robust, modular, and ab initio high-throughput workflow is presented to automatically match and characterize solid–solid interfaces using density functional theory calculations with automatic error corrections. The potential energy surface of the interface is computed in a highly efficient manner, exploiting the high-symmetry points of the two mated surfaces. A database is automatically populated with results to ensure that already available data are not unnecessarily recomputed. Computational parameters and slab thicknesses are converged automatically to minimize computational cost while ensuring accurate results. The surfaces are matched according to user-specified maximal cross-section area and mismatches. Example results are presented as a proof of concept and to show the capabilities of our approach that will serve as the basis for many more interface studies.

1. Introduction

Solid–solid interfaces are ubiquitous in many disciplines of material science, physics, and chemistry, and are essential for many applications, ranging from synthetic antiferromagnets and spintronics [1], battery technology [2] to tribology, especially in nanoelectromechanical systems (NEMS) [3]. Experimental studies of interfaces are very challenging, though, since they are not accessible by many experimental probes due to their inherent nature of being "buried" between two solids. Naturally, simulations do not suffer from these limitations and are uniquely suited to explore solid–solid interfaces. Especially ab initio electronic structure methods are valuable for this task, as they do not depend on a priori knowledge of some or many system parameters and in return can provide information on many significant figures of merit of interfaces, like magnetic interactions [4], thermal properties [5], charge density redistribution [6,7], and tribological properties [8–10].

High-throughput studies have become a valuable tool for material advancements, which are of tremendous importance for many industries and closely tied to various societal challenges like clean energy production [11]. As discussed above, especially for solid–solid interfaces, the cost and trouble of experimentally testing the vast number of possible compounds and alloys that could potentially have beneficial properties are often prohibitive. However, the exponential growth of computer power and the development of efficient data mining and curating techniques using machine learning approaches have opened a new avenue of large-scale computational materials research through high-throughput screening (see [12] and references therein).

In 2018 we have developed a computational framework to harness the great flexibility and predictive power of electronic structure simulations to investigate the tribological properties of homogeneous interfaces of homoatomic materials (analogous to homoepitaxy) [13]. This computational protocol, employing density functional theory (DFT), was used to power high-throughput studies on important tribological figures of merit based on the potential energy surface (PES; also γ-surface or generalized stacking fault energy surface γ_{GSF}) of those interfaces. The PES maps all possible lateral shifts to changes in the system's total energy and thus fixes the adhesion energy as its minimum and one can extract many properties from it. Using it we first studied the fundamental connection of adhesion and frictional forces to charge density redistribution on 31 important examples containing 2D materials, metals, and semiconductors [7]. Later we systematically computed also the shear and cleavage strengths of 106 interfaces comprised from 44 elemental crystals [9]. These works pretty much exhausted our original computational framework, since it was limited

* Corresponding authors.
E-mail addresses: michael.wolloch@univie.ac.at (M. Wolloch), clelia.righi@unibo.it (M.C. Righi).

[1] There were more limitations regarding the Miller indices of the surfaces used to form the interface: For fcc, bcc, and diamond lattices, (100), (110) and (111) orientations were considered, for hcp, only (0001) was possible. Combined with some other limits in the methodology related to the accuracy of pseudo-potentials, we arrived at the 106 interfaces mentioned above.

https://doi.org/10.1016/j.commatsci.2022.111302
Received 13 August 2021; Received in revised form 28 January 2022; Accepted 17 February 2022
Available online 4 March 2022

to homogeneous interfaces of homoatomic materials with either fcc, bcc, hcp, or diamond crystal structures (e.g. Cu(111) on Cu(111)).[1]

Expanding our high-throughput studies to more crystal structures, different surface orientations, and, most important of all, heterogeneous interfaces, is a logical and necessary step, but requires a significantly more involved approach. The additional complexity and the much larger scope of future studies,[2] demand to provide far superior error handling, usability, results' extraction, and functionality. However, the much larger amount of data available using the new tools will allow us to confirm or extend the fundamental relations about charge redistribution, adhesion, and friction we have discovered for homogeneous interfaces.

Another significant difference compared to our past effort is the collection of results in a separate and easily shareable database, which can be easily used to salvage existing results for new analysis and data mining. This is especially useful for other codes that are used to treat interfaces but which depend on pre-defined parameters or classical potentials, which can be trained with the help of ab initio data [14–16].

A major hurdle to overcome is not unique to electronic structure calculations but shared for all atomistic methods using periodic boundary conditions: Constructing a supercell that accommodates both materials forming the interface without imposing unphysical strains. In crystal growth and material deposition, this matching of one crystalline film on another crystalline substrate is known as heteroepitaxy, and algorithms that describe it have existed for more than 35 years, e.g., the one by Zur and McGill [17]. An implementation of this algorithm has been published more recently within the MPInterfaces package [18], and there are ongoing efforts to integrate it tightly into pymatgen (Python Materials Genomics), a very popular library for material analysis [19]. Most approaches are usually geared towards matching a 2D thin film with a substrate, like the very recent work by Zhang et al. [20]. For matching hetero structures of two 2D materials, the coincidence lattice method is also used [21].

A matching cell is not the only requirement to correctly model a solid–solid interface. A priori, it is not clear which lateral relative position of the two matched slabs leads to the highest binding energy and thus to the equilibrium stacking. For that, the whole PES has to be calculated, which is hard to do efficiently for arbitrary matched interfaces. Many results may be derived from the PES, e.g. shear strength and static friction [8,9,13], dynamic friction with the help of some spring models [22,23], or information about dislocation structures and energetics [24]. The ab initio PES of simple systems, such as adsorbed monolayers on metals and bilayer graphene, was very accurately fitted with three-dimensional, analytical functions [23,25], and used in conjunction with atomistic simulations to unravel the origin of fundamental frictional phenomena, such as the onset of frictional slip [26], and the size-dependence of static friction [27,28].

In this paper we will sketch the entire computational protocol that will be released as an open-source package in the near future [29], focusing on the description of efficiently calculating the PES of an already matched interface.

We have decided to implement our work within FireWorks [30], a Python-based high-throughput framework rooted in the Materials Project [31], and use as many pre-engineered pieces of associated packages (such as atomate [32] and pymatgen [19]) as possible. To match the interface, we have modified the approach by MPInterfaces [18] to be better suited for interfaces of two bulk materials instead of a substrate and a thin film. The main change of our implementation with respect to MPInterfaces' is how the unavoidable lattice strain is handled. In the original implementation only one of the materials (the thin-film) get strained, as appropriate for a substrate/thin-film interface. In our work both slabs are strained to fit an averaged lattice. It is possible to weigh this average, and in our workflow, we chose to use the bulk moduli as weights. Thus, if the bulk modulus of material 1 is twice as large as the bulk modulus of material 2, material 2 will be strained twice as much in a hetero interface of these two materials.[3] Another modification includes an automatic initial guess of the interface distance by averaging the spacing between all lattice planes of both slabs forming the interface.

Fireworks is a very mature platform, interfaces very well with the VASP package for DFT calculations [33–35], and provides easy error handling via the custodian package [19]. Of course, other high-throughput platforms based on Python are available (e.g. AiiDA [36,37], pyiron [38], and ASR [39]), and in principle, it should not be hard to port our codes over.

In Section 2 we will give a brief overview of our workflow, its modular structure, and ease of use. In Section 3 we present our workflow for PES calculations in detail and also sketch the other subworkflows we developed to make our computations highly efficient. In both Sections 2 and 3 we will use the interface of cubic WC (Materialsproject ID: mp-13136) and ZnCu (mp-987) as an example to illustrate the new capabilities of our workflow compared to the previously published version [13]. These systems have been chosen as models for technologically important materials, tungsten carbide for cutting tools and coatings, and brass as low friction material for bearings and bushings.

This is followed by some more example results in Section 4 and conclusions and outlook in Section 5. A table highlighting the differences between the current approach and our previous protocol for homogeneous interfaces is given in Section 3 of the supplementary material (SM) [40].

2. Code structure

When writing a fairly complex workflow, such as the one described in this paper, it is of uttermost importance to keep the code modular. This not only allows easy modification and updates to parts of the workflow, but it also makes it possible to generate new workflows with the modular parts. For example, the subworkflows dealing with the convergence of energy cutoff and k-point density (that for our workflow are both used twice, for each of the materials considered) can be used routinely by researchers working with VASP. This is, in principle, independent of high-throughput computations. Another example is the efficient generation of slabs with minimal thickness, speeding up all kinds of surface science studies.

At the same time, the code also has to be robust and as "smart" as possible. In this context, we define robustness as the ability to handle all, or at least nearly all, possible inputs correctly. That means e.g. including the possibility to add van der Waals (vdW) interactions for weakly bound layered systems and local-on site corrections (DFT+U) for correlated systems. Of course, on-the-fly error correction and recovery during DFT calculations is also of imperative importance for high-throughput. In this respect, we rely on the custodian package, which is tightly integrated with FireWorks, atomate, and pymatgen [19], and is able to catch and correct most errors which can routinely happen in VASP calculations.

However, it is always better to avoid errors than to correct them, and so we introduce "smart" methods into our workflows that adapts input parameters based on our expertise in running VASP calculations. We do this by providing specially tuned VASP input sets (based on pymatgen's MPStatic, MPRelax, MPScanStatic, and MPScanRelax sets), which adapt various flags in the input files of VASP to the specific run, with the user only having to select out of a small list of possible

[2] Combining just the 106 different surface slabs in [9] and disregarding all other possible crystal structures and Miller indices would lead to 5565 heterogeneous interfaces. Including 44 more slabs by adding an additional Miller index for each material would lead to more than 11 000 combinations.

[3] Of course, it is also possible to only strain a 2D structure and not the substrate by setting the weight of the 2D material to zero.

self-explanatory keywords like *bulk_full_relax*, *slab_position_relax*, and *interface_scf*. The flags are then optimized to fit the input structure and the task; e.g. wave function projectors might work in real space or in reciprocal space, and the choice depends on system size and the accuracy requirements of the calculation type. The choice of these kinds of parameters, in theory, do not influence the result of a calculation by much, but if cleverly selected, they significantly reduce the chance of errors and also cut down on total computation time.

In Fig. 1 we show a flowchart with the main components of our workflow to compute potential energy surfaces for heterogeneous interfaces. It will be familiar for many computational scientists who have adopted similar strategies for their routine work and possible also automated parts of it. The workflow has a simple structure but is composed of several subworkflows (green rectangles in Fig. 1), which will be detailed in Section 3. More complex logic and decisions are handled there, allowing us to focus on the main features here. In short, even non-specialist users can run these calculations with minimal input and expect correct results due to the decisions automatically made in the subworkflows. The following paragraphs are corresponding directly to Fig. 1:

Reading Input and Initializing: The input parameters are passed to the workflow as a python dictionary. It only has to include very few parameters, mainly the two unique identifiers of the basic bulk structures that should be used (these are Materials IDs from the Materials Project, facilitating an easy search for bulk materials.), the Miller indices for each material to select a slab orientation, if vdW corrections should be used, and the maximal cross-section area of the matched cell. Other parameters, like the functional to be used, can be optionally set; otherwise, default values are used from a central .json file. Bulk structures for both materials are then downloaded from the Materials Project database, transformed into primitive standard structures, and saved in the high-level database. This is the only step where the user of the workflow has to make decisions, namely which systems to use, if vdW corrections should be applied, and if any of the defaults should be replaced by custom parameters (e.g. a different functional or tighter convergence criteria). In high-throughput practice, the input dictionaries will be generally generated automatically from a specific set of structures and their combinations. In our example, the slabs forming the interface are defined as mp-987 with Miller index (110) for ZnCu, and mp-13136 and Miller index (001) for WC. The maximal slab thickness was capped at 12 layers for both systems, vacuum distance between repeating images set to 12 Angstrom, and vdW interactions were not included. Spin polarization was turned on, because although we do not expect spin-polarization for the bulk, at the surfaces or the interface it might occur. In past work, only homoatomic materials of simple cubic, fcc, bcc, hcp, and diamond structures could be considered, while all materials in the Materialsproject database (more than 140 000) can now be used.

Relax shape: The workflow checks the symmetry of the input structure, and in case a non-cubic structure is found, a cell-shape-relaxation with very high energy cutoff and k-point density is performed at constant volume. This ensures that the cell shape (e.g. c/a ratio) is optimized for the selected functional, while the volume will be optimized in the following steps. This subworkflow is not entered by either material in our example, since both are cubic and uniquely defined by a single lattice parameter or the volume.

Converge Energy Cutoff: The energy cutoff is converged with respect to the equilibrium volume and the bulk modulus using subsequent fits to the Birch–Murnaghan equations of state with increasing energy cutoff and very high k-point density. For ZnCu this workflow converges very quickly at 400 eV. For WC, the convergence is equally rapid and an optimal cutoff of 425 eV is selected. The convergence loops start at different values, since the default cutoff for ZnCu is 368.7 eV while the one for WC is 400 eV. Thus the lowest tried values are 375 eV and 400 eV for ZnCu and WC, respectively. In Ref. [13] the convergence loop for all material started at the same cutoff value, generally resulting in more calculations, slower convergence, and occasional total failures due to failed electronic convergence.

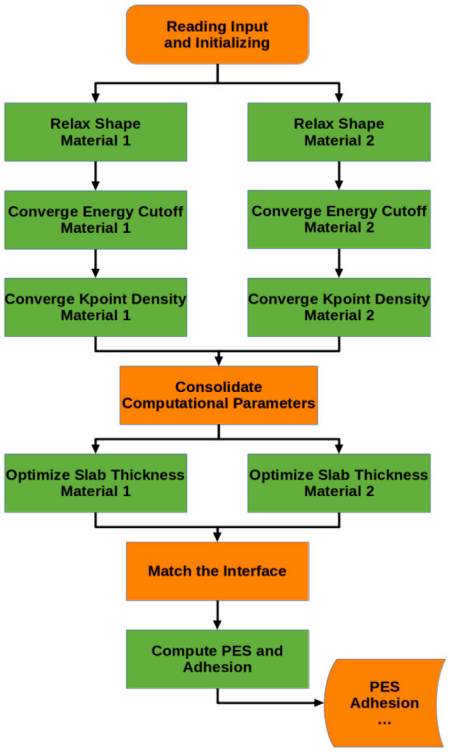

Fig. 1. A flowchart for the full workflow for the creation of potential energy surfaces of heterogeneous systems. Green rectangles denote subworkflows that are also independently usable. Database entries are written at every step, but it is only indicated at the last step since they would otherwise clutter the flowchart.

Converge K-point Density: The density of the k-point mesh is converged in the same way as the energy cutoff since the underlying workflow is identical. The only difference is that the energy cutoff is now kept at the previously converged value, and the k-point density increases until the volume and the bulk modulus converge. The structure at the final equilibrium volume is taken as the bulk reference for the rest of the workflow. For ZnCu the converged value is 5.2 $Å^{-1}$ while it is only 4.1 $Å^{-1}$ for WC. This is not surprising, since the bonding in cubic WC is much more covalent than in ZnCu, and covalently bonded materials tend to require less dense k-point meshes than pure metals. The bulk moduli computed for the materials are 113 GPa for ZnCu and 363 GPa for WC. This fits very well with the values reported by the Materialsproject of 114 and 365 GPa respectively. This proves that calculations for those materials can indeed be done at the lower cutoff values used here compared to the universal 520 eV of standard Materialproject calculations.

Consolidate Computational Parameters: The higher values for the energy cutoff and the k-point density are chosen after all convergence loops have finished so that the interfaces calculations will be both efficient and accurate. In our example case this means that the interface calculations will be done for a plane wave cutoff energy of 425 eV, and a k-point density of 5.2 $Å^{-1}$.

Optimize Slab Thickness: Slabs are built according to the input Miller indices and desired vacuum. Their thickness is converged with respect to the surface energy. A detailed explanation using the examples ZnCu and WC is given in Section 3.2. Here we only note that in our previous protocol for homogeneous interfaces of homoatomic materials, we could only create slabs of very limited Miller indices: 001, 110, and 111, each 6 atomic layers thick. The slab creation was completely hard-coded, while it is now done on the fly for arbitrary Miller indices using pymatgen tools.

Match the Interface: The interface is matched according to chosen limits in strain, differences in angles, and maximal cross-section area. Lattice strain is divided between the two materials depending on the ratio of the bulk moduli. Of course lattice matching did not need to exist in our past work, since we only dealt with homogeneous interfaces were the lattices are the same for the top and bottom slabs. In our example of WC(001) on ZnCu(110), WC has a square unit cell with $a_{WC} = 3.1$ Å, while ZnCu has a rectangular unit cell with $a_{ZnCu} = 2.97$ Å and $b_{ZnCu} = 4.2$ Å. We selected a maximal lattice mismatch of 5% and the algorithm returns a common unit cell achieved by straining a 1×4 supercell of WC, and a 1×3 supercell of ZnCu. This is possible since $a_{WC} \approx a_{ZnCu}$ and $4a_{WC} \approx 3b_{ZnCu}$. Since we have established that WC has a much higher bulk modulus than ZnCu, it gets strained less, −1% in direction a, and 0.4% in direction b, while ZnCu gets strained 3.4% in a and −1.2% in b. The angles are completely preserved however. The cross section area of the matched unit cell is 38.2 Å^2, it contains 126 atoms, and the automatically computed distance between the slabs before relaxation is 1.3 Å.[4]

Compute PES and Adhesion: The PES is calculated by relaxing the slabs in the direction normal to the interface plane for all the unique combinations of high-symmetry points of both surface slabs, duplicating these results to all equivalent points in the interface plane, and interpolating between them with radial basis functions. At the same time, the matched slabs (which generally differ slightly from the previously relaxed unmatched slabs due to strain in the lattice) are fully relaxed. The adhesion for the interface is calculated by subtracting the total energies of the relaxed matched slabs from the total energy of the interface in the lateral position corresponding to the lowest energy.[5] For details and the ZnCu-WC example see Section 3.3

2.1. Output database

Readers familiar with FireWorks will know that it uses MongoDB databases to store workflows, fireworks (smaller workflow units, not to be confused with the package name FireWorks), and calculations. This database has to be installed and configured before FireWorks can be used and is thus a prerequisite for our workflow implementation. We have decided to include a second database layer for our work that stores high-level results only, as frequently done in FireWorks high-throughput studies. This makes it much easier to query results and facilitates sharing the (much smaller) database. We also use this database to avoid duplication of calculations by querying it for previous calculations with the same inputs. For example, bulk convergence for the Fe(110)–Au(111) interface is not needed for the iron part if a Fe(100)-Cu(111) workflow has been already run. The same is, of course, valid for slab relaxations. The integration of these secondary results databases requires minimal additional setup compared to the standard FireWorks installation.

3. Subworkflows

All the workflows described in this section are independent of each other. They can be used in the whole workflow for heterogeneous interfaces shown in Fig. 1, but also in other workflows (e.g. one for homogeneous interfaces, or one that converges computational parameters for a bulk system or the surface energy of a slab).

While we have previously published similar work to converge the k-point density and the energy cutoff [13], and methods to converge slab thickness with respect to the surface energy have also been proposed before [41], we are not aware that the efficient sampling of lateral positions of two slabs with respect to each other has been explored.

3.1. The subworkflows for the conversion of the computational parameters

The size of the supercells needed for heterogeneous interfaces can get pretty big very quickly. Therefore, it is important not to waste resources by imposing unnecessarily large plane-wave energy cutoffs or unnecessarily dense k-point grids. We have thus decided to keep the procedures previously introduced in our work on homogeneous interfaces [13] to converge the energy cutoff and the k point density. We opted to include an input option `n_converge` to tell the subworkflow when it should stop. Setting `n_converge` to n (with $n = 3$ as default) means that convergence is achieved if the last n calculations are within the selected tolerance.

The energy cutoff is converged first by running static calculations of the input bulk structure for five deformations (by default, five different values from −5% to +5% of the input volume) for increasing energy cutoff. The k-point density is kept constant during these runs. By default the high value of 12.5 Å^{-1} is used. The energies are then matched to an equation of state, and the bulk modulus and equilibrium volume are calculated. We can use the bulk modulus workflow already implemented in atomate [32] for this task. Now we increase the energy cutoff and repeat the procedure until both the bulk modulus and the equilibrium volume are converged to the chosen accuracy (by default 0.1% for the volume and 1% for the bulk modulus).[6]

For the k-points convergence, we deviate from the procedure described in [13] where the k-point density is increased until convergence of the total energy is achieved to the desired accuracy. Instead, we perform the same workflow as before for the energy cutoff, thus converging with respect to energy differences and not absolute energies, which leads to smaller meshes and is also physically more meaningful since the absolute energy is meaningless in DFT. The energy cutoff for which this convergence is run can be selected and defaults to the previously converged value if it is present in the database. If not, it is set depending on the functional, 520 eV and 680 eV for PBE and SCAN, respectively. We use Γ-centered meshes exclusively for our systems to avoid problems with oscillating total energies between Γ-centered and Monkhorst–Pack meshes [42].

While running the k-points convergence for cubic tungsten carbide, we see that the on-the-fly error correction manages to recover from some errors for calculations with high volume (+5% strain). For example, for the starting density of 2.0 Å^{-1} the custodian package notices that the highest band is occupied if only the number of bands included by default are considered. The calculation is stopped, an extra band is included, and then it is restarted. The restarted calculation then throws a warning that the RMM-DIIS algorithm for the electrons had problems at one step. Custodian catches the error after the calculation actually has already finished OK, since it only checks every 10 s by default and these calculations are very quick. However, the task is restarted again, now switching to a blocked Davidson iteration scheme. Indeed this EDDRMM warnings of VASP are often a sign of bad convergence and it is generally a good idea to switch the algorithm even if the job might finish correctly since that might take a very long time for larger cells. In any case it is clearly an advantage of our new protocol to include error checking, since the first error would definitely have resulted in wrong results.

For the full workflow for heterogeneous interfaces described in Section 2, we set the respective higher values for the energy cutoff and the k-point density as new computational parameters for the interfaces system as a whole. For a more detailed discussion of this strategy, please see the SM [40].

[4] Reducing the maximally allowed mismatch to 2% as in our other examples, would lead to a significantly larger interface, with a cross section of 174 Å^2 and containing 500 atoms.

[5] Re-relaxing the strained slabs corresponds to explicitly excluding strain energy from the adhesion energy.

[6] We note that often the lattice parameter is used for convergence studies and not the volume. However, using the volume is better suited for a high-throughput framework as ours since non-cubic materials with more than one independent lattice constant can be treated in precisely the same manner.

3.2. Slab generation and thickness convergence

After the computational parameters for a given material have been converged, a slab is constructed from the bulk structure using the approach described in [43] and implemented in pymatgen [19]. This is conceptually done by reorienting the bulk so that the surface plane of interest (identified by a set of Miller indices) is parallel to the x–y-plane, replicating the bulk along the z-direction to make it thicker, and adding a sufficiently thick vacuum layer on top. This vacuum layer is necessary to prevent mutual interactions between the periodic replica of the system in the z-direction and thus correctly simulating semi-infinite surfaces on either side of the slab. Along with the other two lattice directions, the periodic boundary conditions are preserved.

It is necessary to take an adequate number of atomic layers into account due to the reciprocal influence between the two surfaces, which can lead to unwanted quantum phenomena, edge states, and incorrect interactions that would not be present in the semi-infinite surfaces we intend to represent. Choosing unnecessarily thick slabs can lead to computational bottlenecks, significantly increasing the cost of first principle simulations on these systems. Especially since we couple two slabs to form an interface, where the lattices are multiplied laterally to minimize lattice mismatch and the number of atoms can quickly increase ten- or twenty-fold. In that case, each additionally atomic layer considered in excess might add tens of atoms to the interface. Therefore, it is prudent to carefully converge the thickness of the slabs before they are matched, so that the needed accuracy is achieved, but unnecessary thickness is avoided.

To solve this problem, we designed a sub-workflow that creates the slab from a bulk structure and at the same time identifies the minimum optimal thickness needed to simulate it accurately. This is reasonably achieved by converging the surface energy of the slab with the number of layers. Indeed, this value is quite sensitive to the slab thickness due to the surface–surface interaction of thin slabs, but after a certain threshold, the bulk-like region in the middle gets thick enough to stabilize the surface energy.

A certain number of oriented slabs with different thicknesses are created starting from the bulk structure, ranging from a minimum number to a maximum number of atomic layers. Those and the increment in layer number can be changed in the initial input dictionary by the user. Default values are set to 4, 12, and 1 for the minimum, maximum and increment, respectively. Using an increment other than 1 can benefit slowly converging systems or help in the case of uneven layer spacing, e.g. for a diamond 111 slab.

The slabs are then relaxed, and their total energy is calculated from first principles in a separate calculation. This is also done for the oriented bulk, i.e. the bulk cell having the same crystalline orientation of the slabs. The oriented bulk is used instead of a simple bulk cell to ensure that the same k-point meshes are used for the bulk and the slab calculations, which is necessary to get accurate surface energies [41]. Subsequently, the surface energy for the different slabs is calculated as:

$$E_{\mathrm{surf}} = \frac{E_{\mathrm{slab}} - E_{\mathrm{bulk}}\left(N_{\mathrm{slab}}/N_{\mathrm{bulk}}\right)}{2} \tag{1}$$

where E refers to the energy and N to the number of atoms, while the subscripts identify the slab and the oriented bulk.

The convergence is obtained for the thinnest slab presenting a relative difference of its surface energy with respect to the maximum thickness (the reference) below a selected precision threshold, set by default at 1%.

Here we have to note that our current approach does not allow us to discriminate between different surface terminations for equal Miller indices. This means that generally, multi-component crystal structures are not yet handled correctly by this workflow step, unless all surface planes are equivalent. E.g. the (001) and (110) planes of rock-salt-type structures are OK, but the (111) surfaces are not, because they consist of alternating layers for each atom type instead of mixed ones. Additionally, only stoichiometric and symmetric slabs should be used to ensure Eq. (1) is correct. Our example of an ZnCu(110) and WC(001) interface was chosen in a way that those requirements are fulfilled.

We are working on a more general solution that will automatically identify the lowest energy termination for each surface orientation of all periodic crystals regardless of the number of constituents and modify Eq. (1) to be more general, but this is a complex matter which needs further investigation and will be presented in a separate publication. A high-throughput approach for cleavage energies (which in the special case of symmetric slabs are just double the surface energy) has been described recently [44].

It is also important that all the created slabs lead to significant and stable physical systems; otherwise, problems could arise in the convergence loop. This aspect is evident in the oriented bulk case, where the thickness should correspond to the smallest number of layers needed to represent the periodicity of the bulk, e.g., three layers in the case of an fcc crystal along the [111] direction.

After the ideal thickness is found, an additional slab is constructed using an implementation of the LLL algorithm [45] to end up with a slab whose surface normal is as parallel to the cell's z-axis as possible, which makes lattice matching significantly easier. This and all other slabs along with their surface energies are then saved in the high-level database.

For ZnCu(110), convergence with respect to the maximally allowed thickness of 12 layers is reached quickly at five layers (10 atoms; 8.5 Åthick). The surface energy is then, at 1.115 $\mathrm{J/m^2}$, only ∼0.4% smaller than the 12 layer reference of 1.119 $\mathrm{J/m^2}$. Three and four layer thick slabs also are close to the 12 layer case, both showing ∼1.6% smaller surface energy.

For WC(001), the situation is significantly worse, since the surface energy does not converge and the 12 layer thick maximum (24 atoms; 24.7 Å) has to be used. It has a surface energy of 0.61 $\mathrm{J/m^2}$. Additionally some smearing errors occurred during the slab relaxations, but are corrected automatically by custodian. (For metals we use a standard Methfessel–Paxton smearing with a width of $\sigma = 0.2\,\mathrm{eV}$ [46]. Custodian checks if the extrapolated energy for $\sigma \rightarrow 0$ deviate too much from the energy at the current smearing. If this is the case the smearing is reduced.)

A more detailed description of the computational units constituting the sub-workflow, as well as a diagrammatic flowchart, can be found in section 2 and Fig. 2 of the SM [40].

3.3. PES subworkflow

In our past work on homogeneous interfaces, only select crystal structures and surfaces could be considered, and the PES was calculated by sampling pre-defined points for each allowed combination of crystal structure and Miller indices. For heterogeneous interfaces or even homogeneous interfaces with arbitrary surfaces, this approach is not feasible. The method we present here relies instead on symmetry and surface analysis computed on the fly using pymatgen and spglib [19,47]. We illustrate the way the algorithm works using the example of WC(001) and ZnCu(110) slabs:

The top surface of the aligned bottom slab (ZnCu) and the bottom surface of the aligned top slab (WC) that are interacting get analyzed to find all on-top, bridge, and hollow sites using Delaunay triangulation of the topmost (bottommost) atoms. For both materials, seven unique high symmetry sites are found: two on-top positions, three bridge sites (of which two are actually 4-fold hollows, which the triangulation algorithm always classifies as bridge sites), and two 3-fold hollows. This is not surprising, since both surfaces are showing a similar checkerboard pattern. There are a 48 total points for WC and 36 for ZnCu.

The algorithm uses symmetry operations to separate the 7 unique points from the symmetrically equivalent duplicates for each slab. For ZnCu they are the two on top positions of Zn and Cu, respectively, the short bridge between Zn and Cu, the 4 fold hollow at the short Cu–Cu

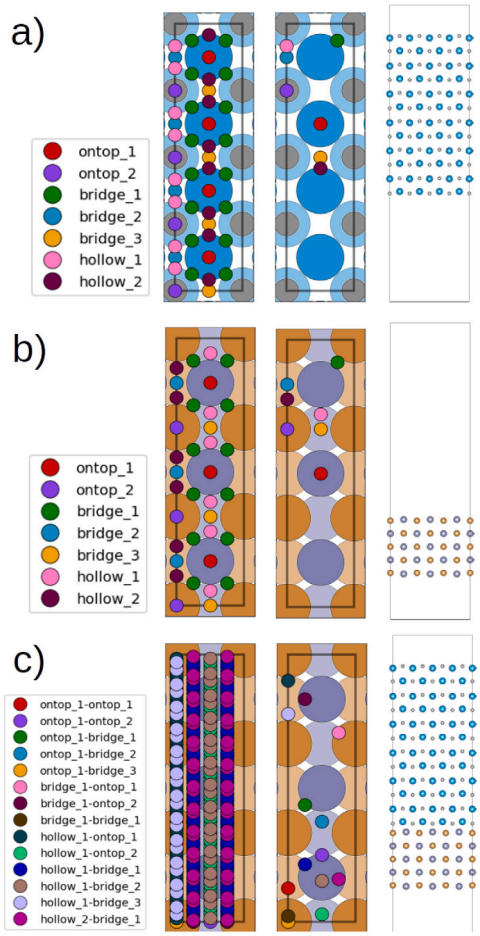

Fig. 2. An overview of the WC(001)-ZnCu(110) interface. (a) Side view of the matched WC slab and the high symmetry points at its bottom. (b) Side view of the matched ZnCu slab and the high symmetry points at its top. (c) All, and unique high symmetry combinations for the combined slabs and side view of the matched interface.

and the long Zn–Zn bridge, and the other 4 fold hollow at the long Cu–Cu and short Zn–Zn bridge. Two more 3 fold hollows are selected at any of the Zn–Zn–Cu and Cu–Cu–Zn possibilities. For WC, the situation is equivalent. See Fig. 2(a) and (b) for a graphical representation.

The unique high symmetry points of both slabs are combined to find the interface's lateral shifts, e.g. `top_1-hollow_1` and `top_1-bridge_2`. Equivalent shifts that may result from the combination of different high-symmetry points get discarded. For the remaining shifts, structures get built and checked for symmetric equivalence (e.g. rotations), and only the truly unique interface structures are kept. This process allows us to reduce the number of combinations in our example from 49 (7 × 7) to 14, since all other combination of shifts are symmetrically equivalent. (See Fig. 2(c)).

These 14 structures are now relaxed using DFT. The atoms are clamped in the directions of the interface plane to ensure that the structure cannot relax back into a total minimum. After the relaxation, static calculations follow to determine accurate adhesion energies for all lateral shifts. Those are than mapped back to all equivalent shifts for all combination of the initially found high symmetry points. In our example we end up with 360 points in the unit cell. This is a very fine sampling of the cell, which we achieve by only calculating 14 points. This means our symmetry based method is ∼26 times more efficient than an regular grid with equivalent spacing.

We now follow the method from our previous work to obtain a two-dimensional continuous function $\gamma(x, y)$, e.g. to plot the PES on a fine grid or evaluate the shear strength [9]. The cell is duplicated laterally

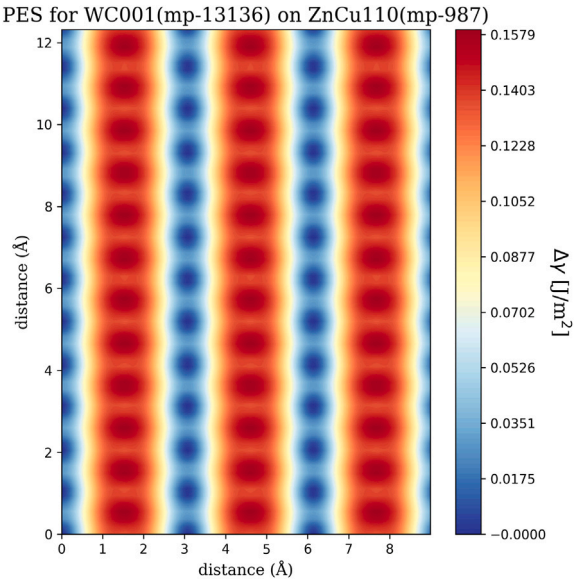

Fig. 3. Potential energy surface (PES) for the WC(001)-ZnCu(110) interface plotted for a 3 × 1 supercell.

to avoid edge effects, and radial basis functions are used to interpolate between the points.

In Fig. 3 we have plotted the PES of our example interface. It is repeated 3 times in the x direction to better show its periodic nature. Note that the periodicity of the PES is much smaller than the unit cell in y-direction. This makes sense intuitively if one thinks about sliding the WC surface (Fig. 2(a)) over the ZnCu substrate (Fig. 2(b)), and remembering that the unit cells are repeated 3 and 4 times in y-direction to match the lattices. Especially in Fig. 2(c) we see that the pattern of equivalent shifts repeats 12 times (3 × 4) in y-direction, while it repeats only once in the x-direction, which is of course visible in the PES.

The adhesion for the interface is $\gamma_{\text{min}} = 1.4\ \text{J/m}^2$, with a rather sizable corrugation $\Delta\gamma = 0.16\ \text{J/m}^2$. However, the main fact we can learn from quickly glancing at Fig. 3 is that the static friction will be very anisotropic, much smaller in y-direction than in x-direction. For more data on the interface, please consult Table 2.

4. Example results

As already stated, this paper intends to present a method and demonstrate its feasibility, not to present a large amount of data. Therefore, alongside the ZnCu-WC example discussed in detail, we only provide a couple of other interfaces centered around aluminum. We have calculated data for the following heterogeneous interfaces: Al(111)–Cu(111), Al(111)–C(111), Al(111)–Fe(110), Al(111)–Al(110), and Al(111)–Al(100), where C denotes the diamond allotrope of carbon.[7] Since some subworkflows produce interesting data on bulk and slabs as well, we will also show those results. All presented data were calculated spin-polarized with VASP version 6.2.0 and the PBE functional. The potential mapping was taken from the pymatgen MPRelax VASP input sets,[8] and the computational parameters have been increased until the equilibrium volume was converged to 0.1% and the bulk modulus to 1%, which was also the convergence criterion for the surface energy. For the interface matching, a cell smaller than

[7] To be clear about the structures we also state the Materials Project IDs in Table 1. The structures used are fcc Al and Cu, bcc Fe, and diamond C.

[8] Since the W_pv potential is requested by the MPRelaxset, but has been depreciated by VASP, it is replaced by the W_sv potential.

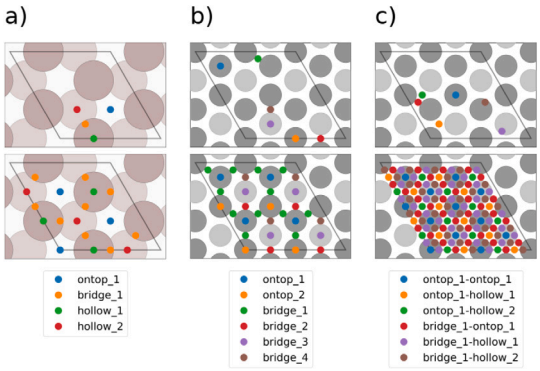

Fig. 4. A overview of the Al(111)–C(111) interfaces high symmetry points. (a) High symmetry points of the bottom of the matched Al slab. (b) High symmetry points on the top of the matched carbon slab. (c) Unique combinations of high symmetry points for the interface, shown on the C slab.

200 Å^2 and a maximum mismatch of 2% was set, alongside a maximum angle difference of 1.5 degrees. However, only one of the investigated interfaces showed any angle strain at all, and that was below 0.1 °. For the WC(001) ZnCu(110) interface, those parameters were slightly relaxed to achieve a smaller unit cell as discussed in Section 2. The tables and figures presented here and in the SM [40] were constructed automatically from the high-level database using Python code from our package.

Fig. 4 shows the high symmetry points of the Al(111)–C(111) interface to illustrate another lattice matching scenario and the corresponding high symmetry point search. Both surfaces have hexagonal symmetry, but the in-plane lattice parameter of Al(111) is about 13% larger than the one for diamond carbon. A reasonable match is found if the Al lattice is rotated by 30° with respect to the carbon lattice, assuming that the a and b lattice vectors start pointing in the same directions. This is a common configuration of matching hexagonal lattices, known as $\sqrt{3}\times\sqrt{3}$ R30, which works here because $2a_{\mathrm{C111}} \simeq \sqrt{3}a_{\mathrm{Al111}}$. The matched lattice is then an average weighted by the bulk moduli of the two materials. Since the bulk modulus of diamond carbon is much higher than the one of fcc Al (see Table 1), the strains we end up with are, for both a and b, much larger for Al(111), at 1.7%, than for C(111), at −0.3% (see Table 2 for details).

Table 1 shows converged bulk moduli, volumes, and lattice parameters and compares them with experimental values. (For cubic WC, we could not find an experimental reference for the bulk modulus unfortunately.) The converged energy cutoffs and k-point densities are also included. For the bulk moduli, we have also shown prediction data taken from the Materials Project and based on statistical learning [48,49]. Those data are inferred from other ab initio data but not directly computed; thus, a somewhat worse fit to experimental values is expected.

The lattice parameters and bulk moduli are plotted against their experimental references in Fig. 5, highlighting their excellent agreement.

In Fig. 6 we present surface energies and compare the results of this work with our previous calculations [13], which were computed with QuantumEspresso [57] and AiiDA [36] for slabs with a fixed thickness of 6 layers. The current work uses optimized thicknesses between four, Fe(110) and Cu(111), and twelve, WC(001), layers (see Table 1 in the SM [40] for all numbers and details).[9] Overall this work is in good agreement with the average literature values, showing some

[9] Obviously we did not consider WC and ZnCu in our past work, so we do not give that data in the comparison here. Our past effort counted the C(111) double layers as single ones; thus the slab was thicker than the one we used here.

Table 1
Bulk properties of Al, Fe, Cu, and C. K is the bulk modulus, a the lattice parameter, E_{cut}^{opt} the optimized cutoff energy, κ^{opt} is the optimized k-point density, and $V^{opt.}$ the volume of the optimized primitive unit cell for each structure. The superscript tw denotes "this work". Experimental data for lattice constants a^{exp} was taken from Ref. [13] and references therein, as well as [50] for ZnCu and [51] for WC, while the reference bulk moduli K^{MP} were queried from the Materials Project database [31]. Experimental bulk modulus data were taken from Ref. [52] for Al, [53] for Fe, [54] for Cu, [55] for C, and [56] for ZnCu.

	Al	Fe	Cu	C	ZnCu	WC
MP-id	mp-134	mp-13	mp-30	mp-66	mp-987	mp-13136
K^{tw} [GPa]	74.329	177.007	140.879	434.689	113.365	363.057
$K^{exp.}$ [GPa]	79.38	164.4–173.5	135.3–144.9	444.24	113.8	–
K^{MP} [GPa]	70.804	215.196	161.358	401.042	120.918	332.213
a^{tw} [Å]	4.045	2.831	3.631	3.573	2.970	4.387
$a^{exp.}$ [Å]	4.049	2.8633	3.615	3.559	2.958	4.192
E_{cut}^{opt} [eV]	225	400	475	475	400	425
κ^{opt} [Å^{-1}]	4.9	3.6	3.7	2.3	5.2	4.1
$V^{opt.}$ [Å^3]	16.545	11.349	11.973	11.403	26.197	21.111

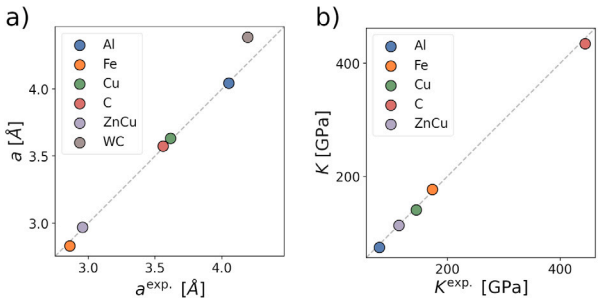

Fig. 5. Converged lattice parameters (a) and bulk moduli (b) with respect to the experimental values.

improvement with respect to our previous results [13] especially for C(111) and Cu(111). The Al(100) and Al(110) are very close in surface energy, although the average values, our past work, and the data from the Materials Project all point to Al(110) to have slightly higher energy. In this work, this order is reversed, with Al(100) having 30 mJ/m^2 higher surface energy than Al(110). We believe that the differences in the code and the pseudopotentials used are a significant factor in the slight variations of results here and note that all results for aluminum lie within one sigma of the literature average.

In Table 2 we show our main results, the data for the heterogeneous interfaces. We present adhesion, corrugation, interfacial separation, cross-section area, and the number of sites in the interface structures. We also give the strains on both lateral lattice vectors and angles of both the top and bottom slabs. In the SM [40], we also provide plots of interface stackings for minimum and maximum configurations, high symmetry points, and PESs.

Of course, it is not easy to compare our results with past work or experimental data here since there is, to our best knowledge, no other work that systematically investigates such metal–metal interfaces. However, we can compare the adhesion energies and the PES corrugation with our past results from homogeneous interfaces [9].

For homogeneous aluminum interfaces, we have previously calculated adhesion energies of 1.52 J/m^2 for the Al(111), 1.84 J/m^2 for Al(100), and 2.13 J/m^2 for the Al(110) interfaces. For the Al(110)–Al(111) interface we get 1.25 J/m^2 and for Al(100)–Al(111) 1.48 J/m^2. This means that both heterogeneous interfaces have less adhesion energy than the homogeneous Al(111) interface, which is not surprising since the stacking is not ideal across the whole interface area for heterogeneous interfaces in contrast to the homogeneous one. Nevertheless, both Al interfaces show adhesion energies close to the Al(111)–Al(111) interface, which is explainable by the prototypical metallic bonding in aluminum that is not much weakened by the interface as long as both

Table 2
Properties of interfaces composed of Al, Cu, Fe, C, WC, and ZnCu slabs with various miller indices where γ_{min} denotes the adhesion energy at the minimum energy configuration, $\Delta\gamma$ the corrugation of the potential energy surface, $\Delta d^{min/max}$ and $HSP^{min/max}$ the interface distances and the matching high symmetry points for the minimum/maximum energy configurations respectively. Values for strain are given in the directions of the two lateral lattice vectors of their respective slabs.

	Al111-Cu111	Al111-Fe110	Al111-C111	Al110-Al111	Al100-Al111	WC001-ZnCu110
γ_{min} [J/m^2]	2.215	3.108	3.049	1.249	1.479	1.415
$\Delta\gamma$ [J/m^2]	0.002	0.135	0.203	0.031	0.038	0.159
Δd^{min} [Å]	2.219	1.818	1.846	2.174	2.194	1.908
Δd^{max} [Å]	2.161	2.105	1.947	2.208	2.464	2.139
Num. sites	78	88	58	186	118	126
HSP^{min}	hollow1-bridge1	ontop1-ontop1	bridge1-ontop1	ontop1-ontop1	hollow2-bridge2	ontop1-bridge3
HSP^{max}	hollow2-ontop1	ontop1-bridge1	ontop1-hollow2	bridge1-ontop1	bridge1-ontop1	ontop1-bridge2
Area [Å^2]	50.751	56.827	21.985	114.521	56.97	38.245
Top strain [%]	[1.18, 1.18]	[−0.72, 0.72]	[1.7, 1.7]	[0.0, −0.99]	[0.07, −0.45]	[−1.01, 0.37]
Bottom strain [%]	[−0.61, −0.61]	[0.3, −0.3]	[−0.29, −0.29]	[0.0, 1.01]	[−0.07, 0.45]	[3.39, −1.16]

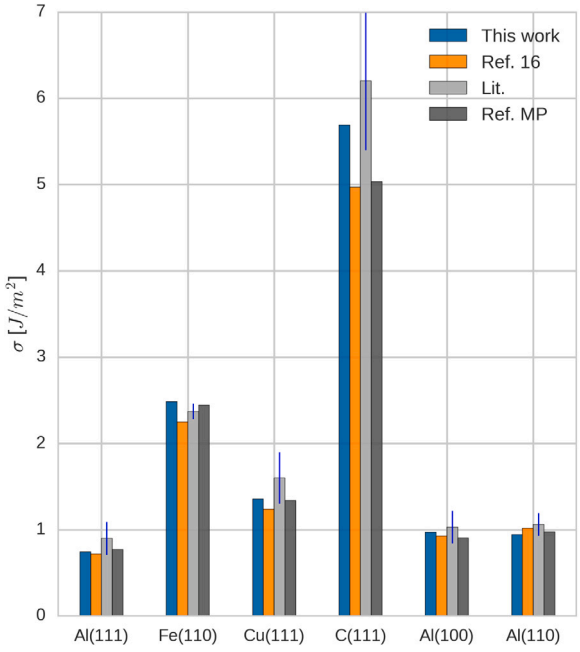

Fig. 6. Surface energies for the monoatomic example slabs. Literature values are averages of previous calculations of various codes and groups (see Ref. [13] and references therein), with the error bars denoting one standard deviation. The Ref. MP values are VASP calculations queried from the Materials Project website [31].

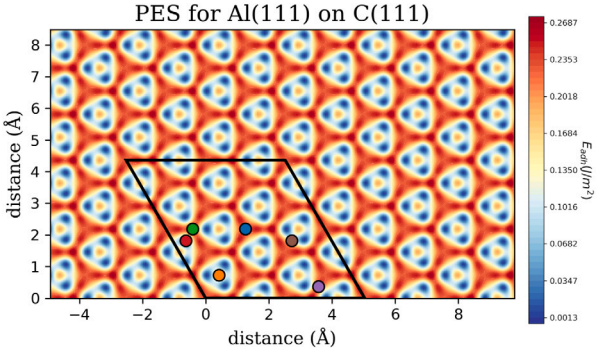

Fig. 7. Potential energy surface (PES) for the Al(111)-C(111) interface. One unit cell including the unique combined high-symmetry points detailed in Fig. 4(d) is also shown.

parts of the interface are reasonably close-packed. At the same time the corrugation $\Delta\gamma$ of those heterogeneous interfaces at 0.04 J/m^2 for Al(100)–Al(111) and 0.03 J/m^2 for Al(110)–Al(111) is reduced by one order of magnitude compared to the homogeneous one for Al(111) at 0.4 J/m^2. This is again explained by the incommensurate stacking of the heterointerfaces. Some parts of the interface stack well, whereas some others do not, at each lateral position, so the total corrugation is comparatively small. However, it should be noted that there are homogeneous interfaces with similarly small $\Delta\gamma$, e.g. the (110) interfaces of the Alkali metals [9].

Some information about the Al(111)-C(111) was already shown in Fig. 4, where the high-symmetry points are plotted. In Fig. 7 we now also show the interpolated PES. It is important to note again that the lattice periodicity is not the periodicity of the PES, as many of the stackings are symmetrically equivalent and thus show the same total energy.

The computed adhesion of 3.0 J/m^2 for Al(111)-C(111) is quite high compared to the other results presented here, as is the corrugation of 0.2 J/m^2. Qi and Hector have previously computed results for the same interface [58], although they do use slightly different strains to match the interface cell. They also do not compute a full PES, but just two different stackings, one of which is an ontop–ontop configuration, while the other is an ontop-bridge one. They report only 0.5% energy difference between those stackings and thus do not compute more. We cannot confirm that result since our calculated PES corrugation is more than 9% of the adhesion energy. The adhesion energy (work of separation in their paper) was computed slightly differently, allowing for full atomic relaxations with constant cell shape, rather than relaxing only the z-direction as we did to ensure a well-defined PES. These full atomic relaxations result in adhesion of 3.98 J/m^2, nearly a third larger than our result. We believe that those relaxations have a larger effect than the lower plane wave cutoff (400 instead of the 475 eV we use), and allowing full relaxations for our minimal PES configurations to compute the adhesion energy is an option we will explore in future work.

For the homogeneous C(111)-C(111) interface we expect a adhesion energy of ~11.4 J/m^2, according to our calculated surface energy for the C(111) slab. Thus we see again that the adhesion of the hetero interface lies in between the homogeneous ones of the constituents.

For Al(111)-Cu(111), we have an adhesion energy of 2.2 J/m^2 which is between the homogeneous limits of Al(111) at 1.5 and Cu(111) at 2.4 J/m^2. However, the PES corrugation is extremely low at 2 mJ/m^2, more than two orders of magnitude smaller than the homogeneous cases. The detailed analysis of this ultra-low corrugation will be done once we implement our analysis of the charge density redistribution [7] and ideal shear strength [8].

The Al(111)-Fe(110) interface is a unique case since the iron slab is magnetic. Indeed also some aluminum atoms carry induced magnetic moments in the relaxed minimum structure, but none higher than 0.3 μ_B. The adhesion is the highest of all interfaces we discuss in this paper, at 3.1 J/m^2, which is not surprising due to the significant adhesion of Fe(110) homogeneous interfaces at 4.95 J/m^2 [9]. Compared to the other heterogeneous interfaces discussed here, the corrugation is high as well, at 0.1 J/m^2. The minimum stacking configuration, with one Al and one Fe atom straight on top of each other, is quite

surprising since metallic bonding usually prefers higher coordination numbers. However, one must be careful with such simple assessments since this ontop–ontop stacking is just realized in a small part of the unit cell. Again, further analysis using charge density differences, which is beyond the scope of this paper, is needed for a proper understanding of the situation.

5. Summary, conclusion, and outlook

We have presented a robust and modular workflow structure to form heterogeneous interfaces of two homo-atomic slabs with arbitrary surface orientations and compute their potential energy surfaces. We have taken care to select computational parameters and slab thicknesses to ensure both efficient computations and accurate results, with minimal required user interaction. At the same time, an easily queryable results database is constructed automatically, which also ensures that no calculations are repeated unnecessarily.

The PES itself is a stepping stone to many other interesting interfacial properties, including adhesion, friction- and fracture-characteristics, dislocation properties, and more. We aim to construct additional modules that can be seamlessly integrated into the current workflow to compute these data for a wide array of interfaces that we will publish in the near future.

Further plans include creating tools to allow the use of arbitrary materials and surface orientations, checking all possible distinct surface termination automatically. Even the reliable automatic calculation of surface energies for such arbitrary slabs is challenging, and the number of possible interface combinations can get quite large quickly. We, of course, will also include analysis of charge densities into our approach to validate our previous findings of their intimate connection to tribological properties of interfaces.

CRediT authorship contribution statement

Michael Wolloch: Methodology, Software, Validation, Investigation, Writing – original draft, Writing – review & editing, Supervision, Project administration, Funding acquisition. **Gabriele Losi:** Methodology, Invesigation,Software, Writing – review & editing, Visualization. **Omar Chehaimi:** Methodology, Investigation, Software, Writing – review & editing. **Firat Yalcin:** Investigation, Software, Data curation, Writing – review & editing, Visualization. **Mauro Ferrario:** Methodology, Validation, Writing – review & editing. **Maria Clelia Righi:** Conceptualization, Methodology, Validation, Writing – review & editing, Supervision, Project administration, Funding acquisition.

Declaration of competing interest

The authors declare that they have no known competing financial interests or personal relationships that could have appeared to influence the work reported in this paper.

Data availability

The raw/processed data required to reproduce these findings cannot be shared at this time as the data also forms part of an ongoing study.

Acknowledgments

These results are part of the SLIDE project that has received funding from the European Research Council (ERC) under the European Union's Horizon 2020 research and innovation program. (Grant agreement No. 865633)

This research was funded in part by the Austrian Science Fund (FWF) [P 32711]. For the purpose of open access, the author has applied a CC BY public copyright license to any Author Accepted Manuscript version arising from this submission.

Appendix A. Supplementary data

Supplementary material related to this article can be found online at https://doi.org/10.1016/j.commatsci.2022.111302.

References

[1] R.A. Duine, K.-J. Lee, S.S.P. Parkin, M.D. Stiles, Synthetic antiferromagnetic spintronics, Nat. Phys. 14 (3) (2018) 217–219, http://dx.doi.org/10.1038/s41567-018-0050-y.

[2] Z. Tu, S. Choudhury, M.J. Zachman, S. Wei, K. Zhang, L.F. Kourkoutis, L.A. Archer, Fast ion transport at solid–solid interfaces in hybrid battery anodes, Nat. Energy 3 (4) (2018) 310–316, http://dx.doi.org/10.1038/s41560-018-0096-1.

[3] B. Bhushan, Nanotribology and nanomechanics in nano/biotechnology, Philos. Trans. R. Soc. Lond. A 366 (1870) (2008) 1499–1537, arXiv:http://rsta.royalsocietypublishing.org/content/366/1870/1499.full.pdf URL http://rsta.royalsocietypublishing.org/content/366/1870/1499.

[4] E. Gerber, Y. Yao, T.A. Arias, E.-A. Kim, Ab initio mismatched interface theory of graphene on $\alpha - RuCl_3$: Doping and magnetism, Phys. Rev. Lett. 124 (2020) 106804, http://dx.doi.org/10.1103/PhysRevLett.124.106804, URL https://link.aps.org/doi/10.1103/PhysRevLett.124.106804.

[5] B. Grabowski, T. Hickel, J. Neugebauer, Ab initio study of the thermodynamic properties of nonmagnetic elementary fcc metals: Exchange–correlation-related error bars and chemical trends, Phys. Rev. B 76 (2007) 024309, http://dx.doi.org/10.1103/PhysRevB.76.024309, URL https://link.aps.org/doi/10.1103/PhysRevB.76.024309.

[6] M. Reguzzoni, A. Fasolino, E. Molinari, M.C. Righi, Potential energy surface for graphene on graphene: Ab initio derivation, analytical description, and microscopic interpretation, Phys. Rev. B 86 (2012) 245434, http://dx.doi.org/10.1103/PhysRevB.86.245434, URL https://link.aps.org/doi/10.1103/PhysRevB.86.245434.

[7] M. Wolloch, G. Levita, P. Restuccia, M.C. Righi, Interfacial charge density and its connection to adhesion and frictional forces, Phys. Rev. Lett. 121 (2018) 026804, http://dx.doi.org/10.1103/PhysRevLett.121.026804, URL https://link.aps.org/doi/10.1103/PhysRevLett.121.026804.

[8] G. Zilibotti, M.C. Righi, Ab initio calculation of the adhesion and ideal shear strength of planar diamond interfaces with different atomic structure and hydrogen coverage, Langmuir 27 (11) (2011) 6862–6867, http://dx.doi.org/10.1021/la200783a, URL http://dx.doi.org/10.1021/la200783a.

[9] M. Wolloch, G. Losi, M. Ferrario, M.C. Righi, High-throughput screening of the static friction and ideal cleavage strength of solid interfaces, Sci. Rep. 9 (1) (2019) 17062, http://dx.doi.org/10.1038/s41598-019-49907-2.

[10] E. Gao, B. Wu, Y. Wang, X. Jia, W. Ouyang, Z. Liu, Computational prediction of superlubric layered heterojunctions, ACS Appl. Mater. Interfaces 0 (0) null, http://dx.doi.org/10.1021/acsami.1c04870, pMID: 34213300.

[11] G. Hautier, A. Jain, S.P. Ong, From the computer to the laboratory: materials discovery and design using first-principles calculations, J. Mater. Sci. 47 (21) (2012) 7317–7340, http://dx.doi.org/10.1007/s10853-012-6424-0.

[12] S. Curtarolo, G.L.W. Hart, M.B. Nardelli, N. Mingo, S. Sanvito, O. Levy, The high-throughput highway to computational materials design, Nature Mater. 12 (2013) 191, http://dx.doi.org/10.1038/nmat3568, EP –, review Article.

[13] P. Restuccia, G. Levita, M. Wolloch, G. Losi, G. Fatti, M. Ferrario, M. Righi, Ideal adhesive and shear strengths of solid interfaces: A high throughput ab initio approach, Comput. Mater. Sci. 154 (2018) 517–529, http://dx.doi.org/10.1016/j.commatsci.2018.08.006, URL http://www.sciencedirect.com/science/article/pii/S092702561830510X.

[14] S. Plimpton, Fast parallel algorithms for short-range molecular dynamics, J. Comput. Phys. 117 (1) (1995) 1–19, http://dx.doi.org/10.1006/jcph.1995.1039, URL http://www.sciencedirect.com/science/article/pii/S002199918571039X.

[15] R.F.L. Evans, W.J. Fan, P. Chureemart, T.A. Ostler, M.O.A. Ellis, R.W. Chantrell, Atomistic spin model simulations of magnetic nanomaterials, J. Phys.: Condens. Matter 26 (10) (2014) 103202, http://dx.doi.org/10.1088/0953-8984/26/10/103202.

[16] A. Vakis, V. Yastrebov, J. Scheibert, L. Nicola, D. Dini, C. Minfray, A. Almqvist, M. Paggi, S. Lee, G. Limbert, J. Molinari, G. Anciaux, R. Aghababaei, S.E. Restrepo, A. Papangelo, A. Cammarata, P. Nicolini, C. Putignano, G. Carbone, S. Stupkiewicz, J. Lengiewicz, G. Costagliola, F. Bosia, R. Guarino, N. Pugno, M. Müser, M. Ciavarella, Modeling and simulation in tribology across scales: An overview, Tribol. Int. 125 (2018) 169–199, http://dx.doi.org/10.1016/j.triboint.2018.02.005, URL http://www.sciencedirect.com/science/article/pii/S0301679X18300756.

[17] A. Zur, T.C. McGill, Lattice match: An application to heteroepitaxy, J. Appl. Phys. 55 (2) (1984) 378–386, http://dx.doi.org/10.1063/1.333084.

[18] K. Mathew, A.K. Singh, J.J. Gabriel, K. Choudhary, S.B. Sinnott, A.V. Davydov, F. Tavazza, R.G. Hennig, Mpinterfaces: A materials project based python tool for high-throughput computational screening of interfacial systems, Comput. Mater. Sci. 122 (2016) 183–190, http://dx.doi.org/10.1016/j.commatsci.2016.05.020, URL http://www.sciencedirect.com/science/article/pii/S0927025616302440.

[19] S.P. Ong, W.D. Richards, A. Jain, G. Hautier, M. Kocher, S. Cholia, D. Gunter, V.L. Chevrier, K.A. Persson, G. Ceder, Python materials genomics (pymatgen): A robust, open-source python library for materials analysis, Comput. Mater. Sci. 68 (2013) 314–319, http://dx.doi.org/10.1016/j.commatsci.2012.10.028, URL https://www.sciencedirect.com/science/article/pii/S0927025612006295.

[20] X.-L. Zhang, J. Pan, X. Jin, Y.-F. Zhang, J.-T. Sun, Y.-Y. Zhang, S. Du, Database construction for two-dimensional material-substrate interfaces, Chin. Phys. Lett. 38 (6) (2021) 066801, http://dx.doi.org/10.1088/0256-307X/38/6/066801, URL http://cpl.iphy.ac.cn/EN/abstract/article_105935.shtml.

[21] D.S. Koda, F. Bechstedt, M. Marques, L.K. Teles, Coincidence lattices of 2d crystals: Heterostructure predictions and applications, J. Phys. Chem. C 120 (20) (2016) 10895–10908, http://dx.doi.org/10.1021/acs.jpcc.6b01496.

[22] S. Cahangirov, C. Ataca, M. Topsakal, H. Sahin, S. Ciraci, Frictional figures of merit for single layered nanostructures, Phys. Rev. Lett. 108 (2012) 126103, http://dx.doi.org/10.1103/PhysRevLett.108.126103.

[23] M. Reguzzoni, A. Fasolino, E. Molinari, M.C. Righi, Friction by shear deformations in multilayer graphene, J. Phys. Chem. C 116 (39) (2012) 21104–21108, http://dx.doi.org/10.1021/jp306929g.

[24] O.N. Mryasov, Y.N. Gornostyrev, A.J. Freeman, Generalized stacking-fault energetics and dislocation properties: Compact versus spread unit-dislocation structures in tial and cuau, Phys. Rev. B 58 (1998) 11927–11932, http://dx.doi.org/10.1103/PhysRevB.58.11927, URL https://link.aps.org/doi/10.1103/PhysRevB.58.11927.

[25] M.C. Righi, M. Ferrario, Pressure induced friction collapse of rare gas boundary layers sliding over metal surfaces, Phys. Rev. Lett. 99 (2007) 176101, http://dx.doi.org/10.1103/PhysRevLett.99.176101, URL https://link.aps.org/doi/10.1103/PhysRevLett.99.176101.

[26] M. Reguzzoni, M. Ferrario, S. Zapperi, M.C. Righi, Onset of frictional slip by domain nucleation in adsorbed monolayers, Proc. Natl. Acad. Sci. USA 107 (2010) 1311–1316, http://dx.doi.org/10.1073/pnas.0909993107, URL http://www.pnas.org/content/107/4/1311.

[27] M. Reguzzoni, M.C. Righi, Size dependence of static friction between solid clusters and substrates, Phys. Rev. B 85 (2012) 201412, http://dx.doi.org/10.1103/PhysRevB.85.201412, URL https://link.aps.org/doi/10.1103/PhysRevB.85.201412.

[28] P. Restuccia, M. Ferrario, P.L. Sivestrelli, G. Mistura, M.C. Righi, Size-dependent commensurability and its possible role in determining the frictional behavior of adsorbed systems, Phys. Chem. Chem. Phys. 18 (2016) 28997–29004, http://dx.doi.org/10.1039/C6CP05386F.

[29] M. Wolloch, G. Losi, O. Chehaimi, M.C. Righi, Triboflow, a python package for high-throughput tribology at interfaces, (to be published).

[30] A. Jain, S.P. Ong, W. Chen, B. Medasani, X. Qu, M. Kocher, M. Brafman, G. Petretto, G.-M. Rignanese, G. Hautier, D. Gunter, K.A. Persson, Fireworks: a dynamic workflow system designed for high-throughput applications, Concurr. Comput.: Pract. Exper. 27 (17) (2015) 5037–5059, http://dx.doi.org/10.1002/cpe.3505, cPE-14-0307.R2.

[31] A. Jain, S.P. Ong, G. Hautier, W. Chen, W.D. Richards, S. Dacek, S. Cholia, D. Gunter, D. Skinner, G. Ceder, K. a. Persson, The materials project: A materials genome approach to accelerating materials innovation, APL Mater. 1 (1) (2013) 011002, http://dx.doi.org/10.1063/1.4812323.

[32] K. Mathew, J.H. Montoya, A. Faghaninia, S. Dwarakanath, M. Aykol, H. Tang, I. heng Chu, T. Smidt, B. Bocklund, M. Horton, J. Dagdelen, B. Wood, Z.-K. Liu, J. Neaton, S.P. Ong, K. Persson, A. Jain, Atomate: A high-level interface to generate, execute, and analyze computational materials science workflows, Comput. Mater. Sci. 139 (2017) 140–152, http://dx.doi.org/10.1016/j.commatsci.2017.07.030, URL https://www.sciencedirect.com/science/article/pii/S0927025617303919.

[33] G. Kresse, J. Hafner, Ab initio molecular dynamics for liquid metals, Phys. Rev. B 47 (1993) 558–561, http://dx.doi.org/10.1103/PhysRevB.47.558, URL https://link.aps.org/doi/10.1103/PhysRevB.47.558.

[34] G. Kresse, J. Furthmüller, Efficiency of ab-initio total energy calculations for metals and semiconductors using a plane-wave basis set, Comput. Mater. Sci. 6 (1) (1996) 15–50, http://dx.doi.org/10.1016/0927-0256(96)00008-0, URL http://www.sciencedirect.com/science/article/pii/0927025696000080.

[35] G. Kresse, J. Furthmüller, Efficient iterative schemes for ab initio total-energy calculations using a plane-wave basis set, Phys. Rev. B 54 (1996) 11169–11186, http://dx.doi.org/10.1103/PhysRevB.54.11169, URL https://link.aps.org/doi/10.1103/PhysRevB.54.11169.

[36] G. Pizzi, A. Cepellotti, R. Sabatini, N. Marzari, B. Kozinsky, Aiida: automated interactive infrastructure and database for computational science, Comput. Mater. Sci. 111 (2016) 218–230, http://dx.doi.org/10.1016/j.commatsci.2015.09.013, URL http://www.sciencedirect.com/science/article/pii/S0927025615005820.

[37] S.P. Huber, S. Zoupanos, M. Uhrin, L. Talirz, L. Kahle, R. Häuselmann, D. Gresch, T. Müller, A.V. Yakutovich, C.W. Andersen, F.F. Ramirez, C.S. Adorf, F. Gargiulo, S. Kumbhar, E. Passaro, C. Johnston, A. Merkys, A. Cepellotti, N. Mounet, N. Marzari, B. Kozinsky, G. Pizzi, Aiida, 1.0. A scalable computational infrastructure for automated reproducible workflows and data provenance, Sci. Data 7 (1) (2020) 300, http://dx.doi.org/10.1038/s41597-020-00638-4.

[38] J. Janssen, S. Surendralal, Y. Lysogorskiy, M. Todorova, T. Hickel, R. Drautz, J. Neugebauer, Pyiron: An integrated development environment for computational materials science, Comput. Mater. Sci. 163 (2019) 24–36, http://dx.doi.org/10.1016/j.commatsci.2018.07.043, URL http://www.sciencedirect.com/science/article/pii/S0927025618304786.

[39] Atomic simulation recipes, 2021, https://asr.readthedocs.io/en/latest/index.html (accessed: 2021-06-29).

[40] See Supplemental Material at https://doi.org/10.1016/j.commatsci.2022.111302 which includes Refs. [13,30–32] for: Additional details and explanation about the slab thickness convergence subworkflow; a table with surface energy results for the slab calculations; several figures for interface stackings and PES plots.

[41] W. Sun, G. Ceder, Efficient creation and convergence of surface slabs, Surf. Sci. 617 (2013) 53–59, http://dx.doi.org/10.1016/j.susc.2013.05.016, URL http://www.sciencedirect.com/science/article/pii/S003960281300160X.

[42] H.J. Monkhorst, J.D. Pack, Special points for brillouin-zone integrations, Phys. Rev. B 13 (1976) 5188–5192, http://dx.doi.org/10.1103/PhysRevB.13.5188, URL http://link.aps.org/doi/10.1103/PhysRevB.13.5188.

[43] R. Tran, Z. Xu, B. Radhakrishnan, D. Winston, W. Sun, K.A. Persson, S.P. Ong, Surface energies of elemental crystals, Sci. Data 3 (2016) 160080, http://dx.doi.org/10.1038/sdata.2016.80, URL https://www.nature.com/articles/sdata201680.

[44] A. Palizhati, W. Zhong, K. Tran, S. Back, Z.W. Ulissi, Toward predicting intermetallics surface properties with high-throughput dft and convolutional neural networks, J. Chem. Inf. Model. 59 (11) (2019) 4742–4749, http://dx.doi.org/10.1021/acs.jcim.9b00550, pMID: 31644279.

[45] A.K. Lenstra, H.W. Lenstra, L. Lovász, Factoring polynomials with rational coefficients, Math. Ann. 261 (4) (1982) 515–534, http://dx.doi.org/10.1007/BF01457454.

[46] M. Methfessel, A.T. Paxton, High-precision sampling for brillouin-zone integration in metals, Phys. Rev. B 40 (1989) 3616–3621, http://dx.doi.org/10.1103/PhysRevB.40.3616, URL https://link.aps.org/doi/10.1103/PhysRevB.40.3616.

[47] A. Togo, I. Tanaka, Spglib: a software library for crystal symmetry search, 2018, arXiv:1808.01590.

[48] M. de Jong, W. Chen, T. Angsten, A. Jain, R. Notestine, A. Gamst, M. Sluiter, C. Krishna Ande, S. van der Zwaag, J.J. Plata, C. Toher, S. Curtarolo, G. Ceder, K.A. Persson, M. Asta, Charting the complete elastic properties of inorganic crystalline compounds, Sci. Data 2 (1) (2015) 150009, http://dx.doi.org/10.1038/sdata.2015.9.

[49] M. de Jong, W. Chen, R. Notestine, K. Persson, G. Ceder, A. Jain, M. Asta, A. Gamst, A statistical learning framework for materials science: Application to elastic moduli of k-nary inorganic polycrystalline compounds, Sci. Rep. 6 (1) (2016) 34256, http://dx.doi.org/10.1038/srep34256.

[50] S.S. Rao, T.R. Anantharaman, Constitution of brasses below 500 ° C, Int. J. Mater. Res. 60 (4) (1969) 312–315, http://dx.doi.org/10.1515/ijmr-1969-600411.

[51] A.M. Nartowski, I.P. Parkin, M. MacKenzie, A.J. Craven, I. MacLeod, Solid state metathesis routes to transition metal carbides, J. Mater. Chem 9 (1999) (1999) 1275–1281, http://dx.doi.org/10.1039/A808642G.

[52] G.N. Kamm, G.A. Alers, Low-temperature elastic moduli of aluminum, J. Appl. Phys. 35 (2) (1964) 327–330, http://dx.doi.org/10.1063/1.1713309.

[53] A.P. Jephcoat, H.K. Mao, P.M. Bell, Static compression of iron to 78 gpa with rare gas solids as pressure-transmitting media, J. Geophys. Res.: Solid Earth 91 (5) (1986) 4677–4684, http://dx.doi.org/10.1029/JB091iB05p04677, arXiv:https://agupubs.onlinelibrary.wiley.com/doi/pdf/10.1029/JB091iB05p04677 URL https://agupubs.onlinelibrary.wiley.com/doi/abs/10.1029/JB091iB05p04677.

[54] H.M. Ledbetter, E.R. Naimon, Elastic properties of metals and alloys, ii. copper, J. Phys. Chem. Ref. Data 3 (4) (1974) 897–935, http://dx.doi.org/10.1063/1.3253150.

[55] A. Migliori, H. Ledbetter, R.G. Leisure, C. Pantea, J.B. Betts, Diamond's elastic stiffnesses from 322 k to 10 k, J. Appl. Phys. 104 (5) (2008) 053512, http://dx.doi.org/10.1063/1.2975190.

[56] P.L. Young, A. Bienenstock, Elastic constants of β-brass from room temperature to above 520°C, J. Appl. Phys. 42 (7) (1971) 3008–3009, http://dx.doi.org/10.1063/1.1660668.

[57] P. Giannozzi, S. Baroni, N. Bonini, M. Calandra, R. Car, C. Cavazzoni, D. Ceresoli, G.L. Chiarotti, M. Cococcioni, I. Dabo, A.D. Corso, S. de Gironcoli, S. Fabris, G. Fratesi, R. Gebauer, U. Gerstmann, C. Gougoussis, A. Kokalj, M. Lazzeri, L. Martin-Samos, N. Marzari, F. Mauri, R. Mazzarello, S. Paolini, A. Pasquarello, L. Paulatto, C. Sbraccia, S. Scandolo, G. Sclauzero, A.P. Seitsonen, A. Smogunov, P. Umari, R.M. Wentzcovitch, Quantum espresso: a modular and open-source software project for quantum simulations of materials, J. Phys.: Condens. Matter 21 (39) (2009) 395502, http://dx.doi.org/10.1088/0953-8984/21/39/395502.

[58] Y. Qi, L.G. Hector, Adhesion and adhesive transfer at aluminum/diamond interfaces: A first-principles study, Phys. Rev. B 69 (2004) 235401, http://dx.doi.org/10.1103/PhysRevB.69.235401, URL https://link.aps.org/doi/10.1103/PhysRevB.69.235401.